**ORIGINAL ARTICLE**

# Design and Simulation of a Novel Tunable Terahertz Biosensor Based on Metamaterials for Simultaneous Monitoring of Blood and Urine Components

Hamed Emaminejad[1] · Ali Mir[1] · Ali Farmani[1]

## Abstract

In this essay, a tunable metamaterial-based biosensor is proposed for simultaneous monitoring of blood components including cells, plasma, water, thrombus, and urine components as well as glucose, albumin, and urea. The proposed biosensor is based on optical sensors, and it provides real-time, label-free, and direct detection, small size, and cost-effectiveness that can be an alternative tool to other conventional methods. The influence of operating frequency, sample thickness, temperature, and radiation angle on the performance of the sensor is investigated by the finite element method (FEM). Numerical results show that the maximum sensitivity and figure of merit (FoM) in the high frequency are 500 (nm/RIU) and 2000, and for low frequency are 136 (μm/RIU) and 155, respectively. The footprint of the structure is 0.34 μm2, which is remarkably smaller than the other reported biosensing structures. The proposed biosensor has the potential to provide high sensitivity, high FoM, and a wide operating range for biomedical applications.

**Keywords** Nano-biosensor · Biomaterial · Biosensor · Metamaterial · Blood

## Introduction

Today, prostate cancer is one of the most common diseases in men, especially adults. This disease may not appear in the early stages; in more advanced stages, it can cause problems in urinating, blood in the urine, or pain in the pelvic and waist regions during urination. Another symptom that occurs later is the low level of red blood cells [1–11]. For these reasons, the use of extremely accurate and rapid biosensors can be very useful in examining the components of blood and urine. Biosensors are highly effective tools for clinical and diagnostic, industrial, environmental monitoring, food industry, and so on [12–23]. The biosensor must be very accurate, highly sensitive, and show linear behavior relative to different concentrations. They should be small and not damage biological tissue for use in clinical trials. Also, a biosensor must perform real-time analysis that can be used to quickly measure analytes from human samples. The analyte should be stable and specific under normal storage conditions, and the biosensor must be portable, cost-effective, small, and usable by semi-skilled operators. They have several types including electrochemical, amperometric, potentiometric, thermometric, optical, and luminescent [24–33]. Amongst these, optical sensors are good candidates because of their high sensitivity, portability, sample-free label, and low-cost and high-speed for sample preparation [34–37]. The main problems of optical biosensors are related to the interaction of biological molecules with the sensor surface, as well as their integration for making small devices. The environmental monitoring sensors with high sensitivity are other important sensors. Based on their structure, optical sensors include different types such as photonic crystals [38, 39], metamaterials (MMs) [40, 41], optical fibers [42], plasmon-induced transparency [43], and so on [44–64]. The unique properties of MMs are the negative refractive index and confining electromagnetic waves [65, 66]. MMs were introduced theoretically in 1968 by the Russian physicist Victor Veselago. Unlike natural materials, MMs can have a negative refractive index; therefore, they are not found in nature. To achieve such a structure, we use a combination of resonators (with negative $\mu$) and an array of thin metal wires (with negative $\varepsilon$), which ultimately leads to a negative refractive index ($n = \sqrt{\epsilon\mu}$). MMs have many

✉ Ali Farmani
Farmani.a@lu.ac.irc

1 School of Electrical and Computer Engineering, Lorestan University, Khoramabad, Iran

advanced applications such as cloaking [67], miniature antenna [68–74], superlens [75], absorber [76], and so on [13, 56, 77–87]. In several works, MMs are used as a biosensor for the detection of biological tissues. Typically, the main components of MMs are resonators, which have a certain resonance frequency according to their shape and size [88]. The MM biosensors in terms of their operating frequency regime are divided into several groups of microwave [89], terahertz [90], and plasmonic [91]. As the frequency rises, the sensor's dimensions become smaller [15, 92–94]. Thus, they will be able to detect samples with a very small thickness (at nanoscale) [95]. Also, MM biosensors can be used to detect DNA [96], cancer cells [97], and microfluidic applications [40] among other uses. The main factor for detecting the above-mentioned cases is the variation of the dielectric constant of under test cells. For example, a cancerous cell has more water content than a normal cell, which results in a higher dielectric constant and electrical conductivity [98]. Also, blood components such as blood plasma, cells, clots, and water have a certain refractive index. About 55% of blood is made up of plasma, and the rest includes red and white cells and also platelets [99]. The dielectric constant also changes with glucose concentration in blood (or urine) [100]. Therefore, it is the main parameter for detecting glucose concentration. In this regard, several research groups have examined the changes in dielectric constant at different concentrations of glucose-based spectroscopy [101]. For instance, in Robinson and Dhanlaksmi [102], a photonic crystal biosensor is provided to detect the concentration of glucose, albumin, and urea in urine at 1550-nm wavelength. Tao et al. [103] measured experimentally the concentration changes of glucose and urea in the water using MM-based biosensors. MMs used in this work have a substrate of paper. This feature partly defines the practical aspects of this detection method. From a practical perspective, some of these structures suffer from a serious problem, i.e., their big footprint and labeled material detection, which leads to high-cost products [104–113].

In the present works, a MM biosensor structure is designed based on split-ring resonators (SRRs), in which the operating frequency regime can be easily tuned by changing the size of the system or incident angle. The main mechanism of the proposed structure is based on the shift in the resonance frequency. Besides, to show their diagnosis ability, the variations in the transmission and reflection amplitude of waves have been investigated. One of the main advantages of our proposed sensor is the tunability of operation frequency. Hence, the proposed sensor is evaluated for low-frequency operations (1–2 THz) and high-frequency operations (around 193 THz), which perfectly reflect the trait of the tunable sensor. As will be discussed later, environmental parameters such as temperature and thickness of the samples can affect the response and performance of the sensor. Therefore,

mentioned parameters can be well controlled under laboratory conditions. For computer simulations, a proper physical model is needed for biological tissues. One of the widely used models for this purpose is the Debye model. Finite-element-method (FEM) is applied to calculate the partial differential equations (PDEs) in 3D space. Numerical results show that the maximum sensitivity and figure of merit (FoM) in the high frequency are 500 (nm/RIU) and 2000, and for low frequency are 136 (µm/RIU) and 155, respectively. This study provides a path for the development of novel nano-scale practical biomedical applications.

## The Physical Structure and Operation of the Proposed Sensor

In this section, the geometrical parameters of the proposed structure are presented. As we know, the base and foundation of the MM structures are the resonators, which have different geometric shapes. The most common resonator in this regard is the split ring-resonator (SRR). A metal (e.g., copper and gold) resonator is placed on an insulator substrate. Our suggested biosensor structure is based on frequency-selective-surface (FSS) filters. Figure 1a presents an overview of an FSS that includes arrays of SRRs that are located on a sub-layer. The waves fall in the direction of the red arrow. The resonators resonate at a specific frequency, depending on their size and shape, and pass or filter a particular frequency. The main sensor structure is shown in Fig. 1b. Here, the resonator structure is in the form of the square that is located on a Teflon (PTFE) substrate with a dielectric constant of 2.1. Also, we used a perfectly matched layer (PML) to confine the areas of mathematic computational in the simulation process for open- boundary problems.

For the sake of simplicity, the periodic boundary conditions in the FEM analysis, which refer to repeated cells, are considered. The basis of detection in this method is the variation in the refractive index of analytes that are placed on the sensor. Our analytes here are blood and urine. Changes in the level of glucose (urea or albumin) result in the refractive index change of the blood (urine). The proposed sensor has resonators with a specific resonance frequency under normal conditions (without any sample), which is a function of the environmental refractive index. Now, if an analyte is placed on the sensor, the resonance frequency of the sensor will shift. The main objective of this paper is to diagnose blood components such as whole blood, blood cells, blood plasma, thrombus, and water. Also, the concentrations of glucose in the blood and urine, albumin, and urea in urine are calculated. In the next section, we will examine the optical properties of these tissues.

**Fig. 1** (**a**) The overall schematic of a FSS. (**b**) An overview of the array structure of the biosensor



**(a)**

**(b)**
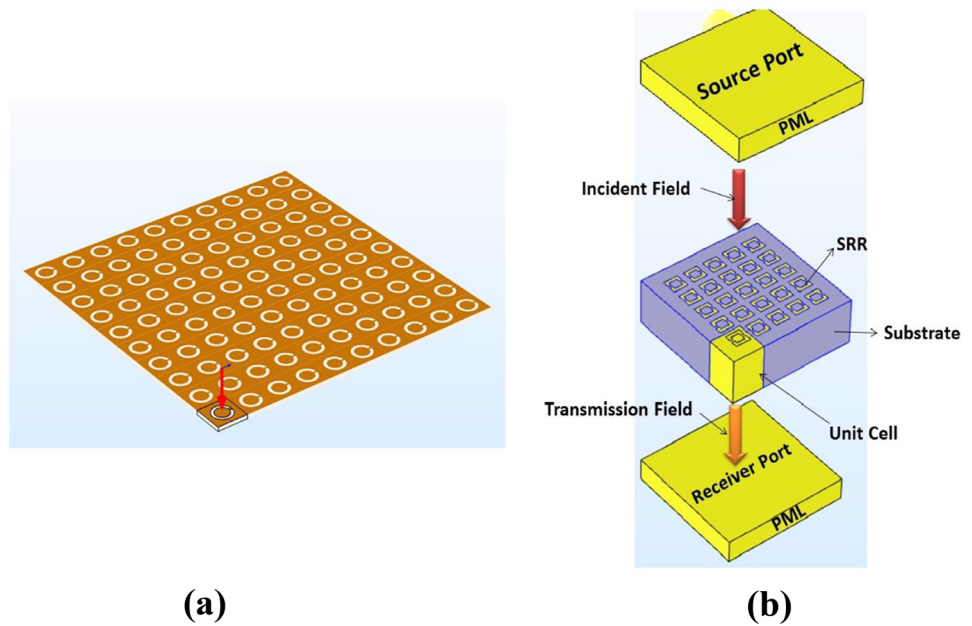
## Fundamental Modeling Data

This section examines the parameters and models that are needed to simulate the biological tissues such as blood and urine components. The biological models are expressed in two frequency ranges from 0.2 to 2 THz (low frequency) and around 193 THz (high frequency). There are two reasons for using high- and low-frequency modes: First, the biosensor can be easily tuned by an only change in the sensor's unit cell size. Second, the sensor operation at low and high frequencies resolves many challenges. Also, for the mentioned frequency ranges, the experimental refractive index and the dielectric constant of the samples are available. Debye parameters of blood components (BCs) in the 0.2–2 THz regime were extracted from [114].

### Modeling of Bio-tissues in the 0.2–2 THz

In this work, the Debye model is used to reveal blood components such as whole blood, blood cells, blood plasma, thrombus, and water, as follows:

$$\varepsilon(\omega) = \varepsilon_\infty + \sum_{n=1}^{i} \frac{\Delta\varepsilon}{1 + j\omega\tau_n} = \varepsilon_\infty + \frac{\varepsilon_s - \varepsilon_2}{1 + j\omega\tau_1} + \frac{\varepsilon_2 - \varepsilon_\infty}{1 + j\omega\tau_2} \tag{1}$$

where $\varepsilon_\infty$ is the real part of the permittivity at a high-frequency limit, $\varepsilon_s$ and $\varepsilon_2$ are static limit permittivity and intermediate dielectric value, $\tau_1$ and $\tau 2$ are relaxation times of the first and second relaxation process, and ω is the angular frequency. The values of these parameters are shown in Table 1 for blood components in the range of 0.2—2 THz [114].

The Debye parameters of single-pole are extracted from [115] according to the glucose concentration in the blood plasma for amounts from 0 to 16,000 (mg/dl).

### Modeling of Bio-tissues at High Frequency (1550 nm)

In the following, the concentration of glucose in blood and concentrations of glucose, albumin, and urea in urine are studied. For this purpose, the variation of the refractive index is considered. The refractive indices and electrical conductivities for various concentrations at high frequencies (about 193 THz) are taken from. Considering these values, it is observed that by changing the concentration, the refractive index changes from 1.335 to 1.348. The electrical conductivity values are taken into account for losses, which are modeled as follows [44]:

$$N = n + ik \equiv \sqrt{\epsilon_r} \tag{2}$$

**Table 1** Debye parameters belong to blood components in the 0.2–2 THz regime [114]

| $\tau_2 (ps)$ | $\tau_1 (ps)$ | $\varepsilon_2$ | $\varepsilon_s$ | $\varepsilon_\infty$ | Blood components |
|---|---|---|---|---|---|
| 0.1 | 14.4 | 3.8 | 130 | 2.1 | Whole Blood |
| 0.1 | 16.1 | 3.7 | 130 | 2.2 | Thrombus |
| 1.8 | 410.8 | 23.8 | 2.5 | 3.4 | Blood Cells |
| 0.1 | 8.0 | 3.6 | 78.8 | 1.7 | Blood Plasma |
| 0.1 | 8.4 | 4.5 | 78.8 | 3.3 | Water |

$$n = \sqrt{\frac{|\epsilon_r| + \epsilon'_r}{2}}, \ k = \sqrt{\frac{|\epsilon_r| - \epsilon'_r}{2}} \qquad (3)$$

$$\epsilon_r = \epsilon'_r - i\epsilon''_r = \epsilon'_r + i\frac{\sigma}{\omega\epsilon_0} \qquad (4)$$

where $n$ and $k$ are real and imaginary parts of the refractive index, respectively; $\sigma$ refers to the electrical conductivity of the material; and $\epsilon0$ is the vacuum dielectric constant.

According to the above data, the resonant frequency of the proposed sensor is set in the low frequency (0.2–2 THz) and high frequency (around 193 THz). The results are discussed in the next section.

## Results

### Low Frequency

In this section, we set the frequency resonance of the system to operate at the frequency range of 0.2–2 THz. Figure 2a shows the accurate dimensions of the sensor unit cell. Figure 2b presents the frequency response of the system.

The blue and red graphs are related to the transmittance and reflectance of the stricter, respectively. The system, in this case, has a resonant frequency, about 1.94 THz.
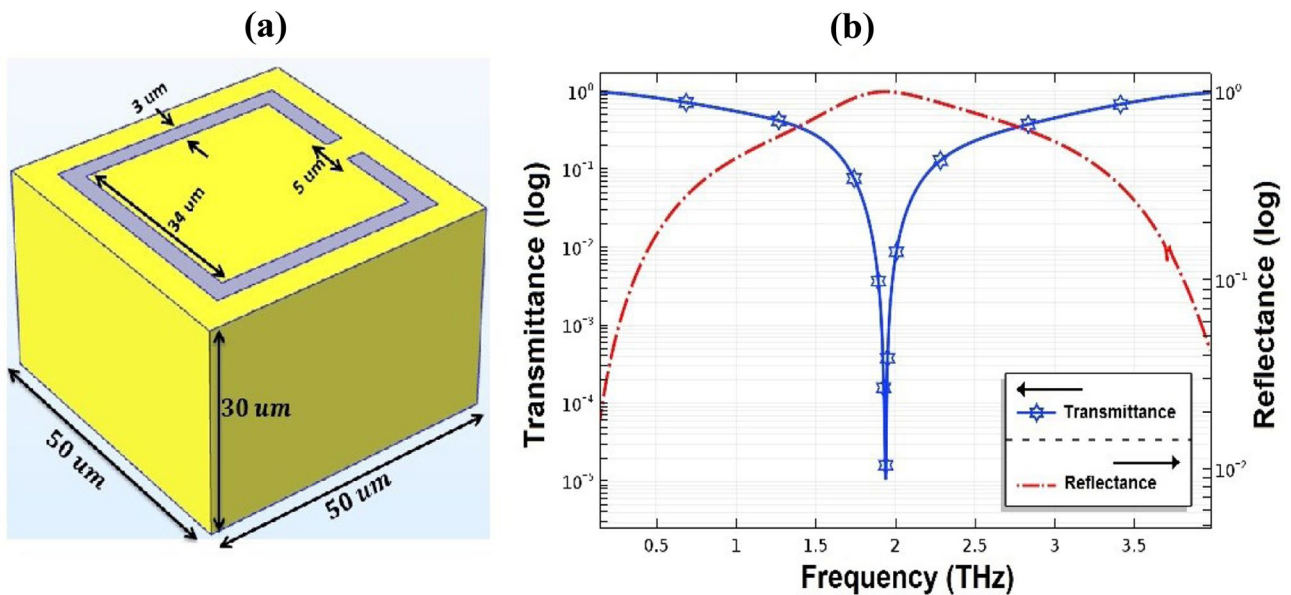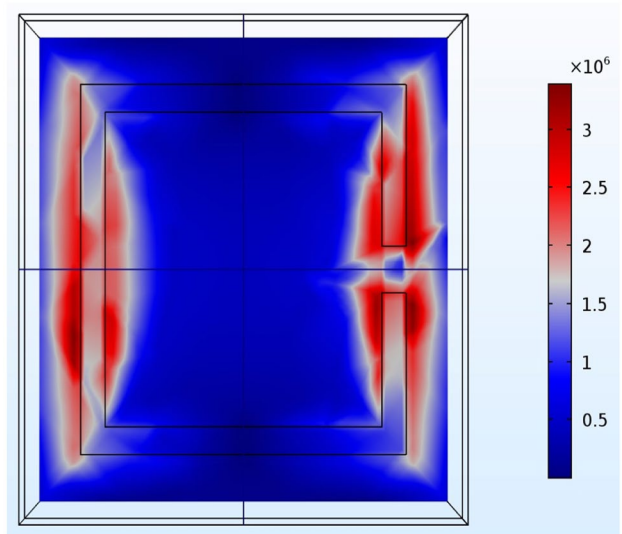
**Fig. 3** Electric field distribution at the frequency of $f = 1.94$ THz

Figure 3 shows the distribution of the electric field at the resonant frequency (1.943 THz) of the system.

By placing samples on the sensor, consider into account their dielectric constants, a blue shift occurred at the resonant frequency. Figure 4 presents the frequency response variations for different blood components. The lower and higher resonant frequencies correspond to the blood plasma (1.55 THz) and water (1.37 THz), respectively.
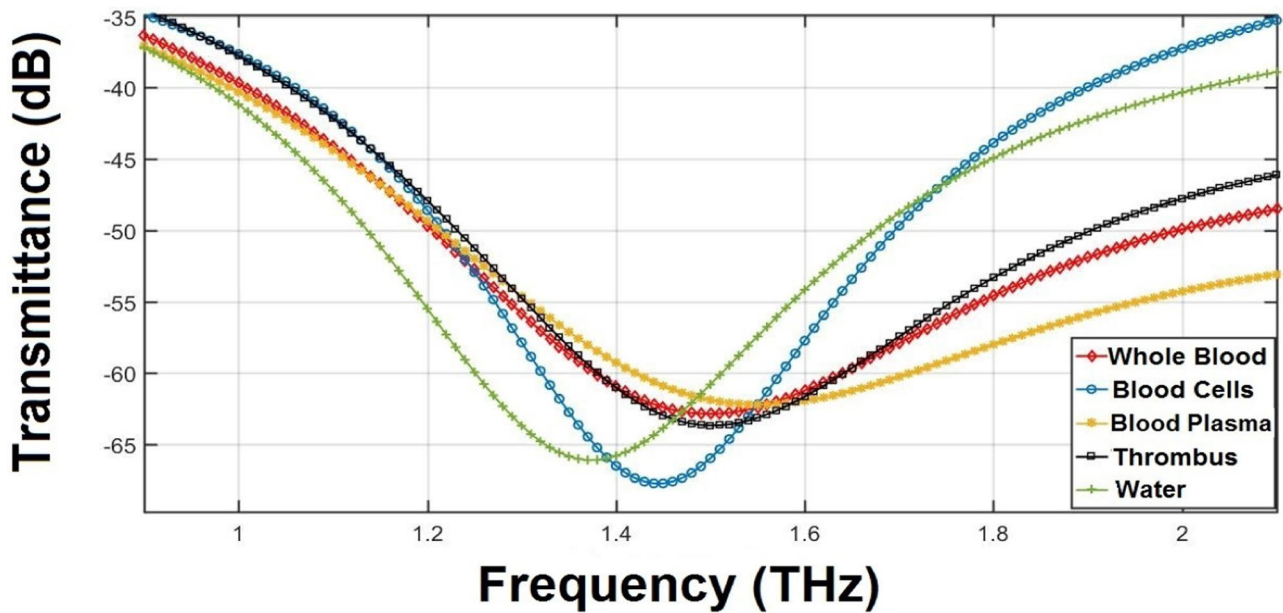
**(a)**                                                    **(b)**

**Fig. 2** **(a)** Structure and dimensions of the proposed sensor unit cell for operation at the low-frequency regime. **(b)** Frequency response of the proposed sensor at the low-frequency regime

**Fig. 4** Variation in the resonance frequency of the system for different blood samples

Figure 5 shows the frequency response of the sensor for different glucose densities in the blood plasma.

The dielectric constant is changed via different glucose concentration, and, therefore, various frequency response is met. Considering no sample state, the minimum and maximum frequency shifts correspond respectively to 1000 and 16,000 mg/dl with the resonance frequency of these concentrations being 1.82 and 1.12 THz.

## High Frequency (About 193 THz)

As the operating frequency of the system increases, the dimensions of resonators diminish. Figure 6 presents the unit cell dimensions of the proposed sensor for working near the 193 THz frequencies. The sub-layer used here is Teflon, which has a refractive index of 1.34.
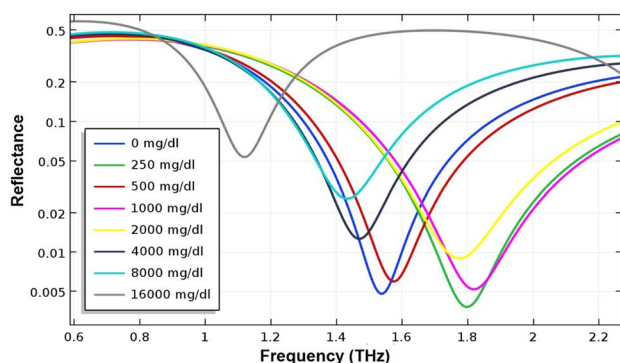


**Fig. 5** Frequency response of the sensor as a function of the concentration of glucose in the blood plasma

The transmittance and reflectance diagrams of the sensor for frequencies around 193 THz are shown in Fig. 7. The accurate value of the resonant frequency of the system is 193.4 THz (1550 nm). Figure 8 also illustrates the distribution of the electric field at a frequency of 193.4 THz.

Figure 9 shows the change of the resonance frequency as a function of the blood glucose, urine glucose, albumin, and urea concentrations. As can be seen, with increasing the concentration of these parameters in blood and urine, the resonance frequency of the system shifts to lower frequencies. Although the difference in the refractive indices is very low ($\Delta n = 0.001$), as can be seen, the graphs of each of the concentrations are separated by a good resolution. The minimum resolution between the concentrations is 0.01 THz. The lowest and highest shifts in the frequency response of the system are related to the refractive index of 1.35 (normal concentrations) and 1.348 (10 mg/dl), respectively. The resonant frequency values for these concentrations are 191.6 and 190.81 THz, respectively.

## Effective Parameters on the System Response

### Thickness of Samples

The thickness of the placed samples on the sensor can somewhat affect the response of the system. Figure 10 depicts the frequency response of the system for different thicknesses of the whole blood. As can be seen, by increasing the sample thickness, the system
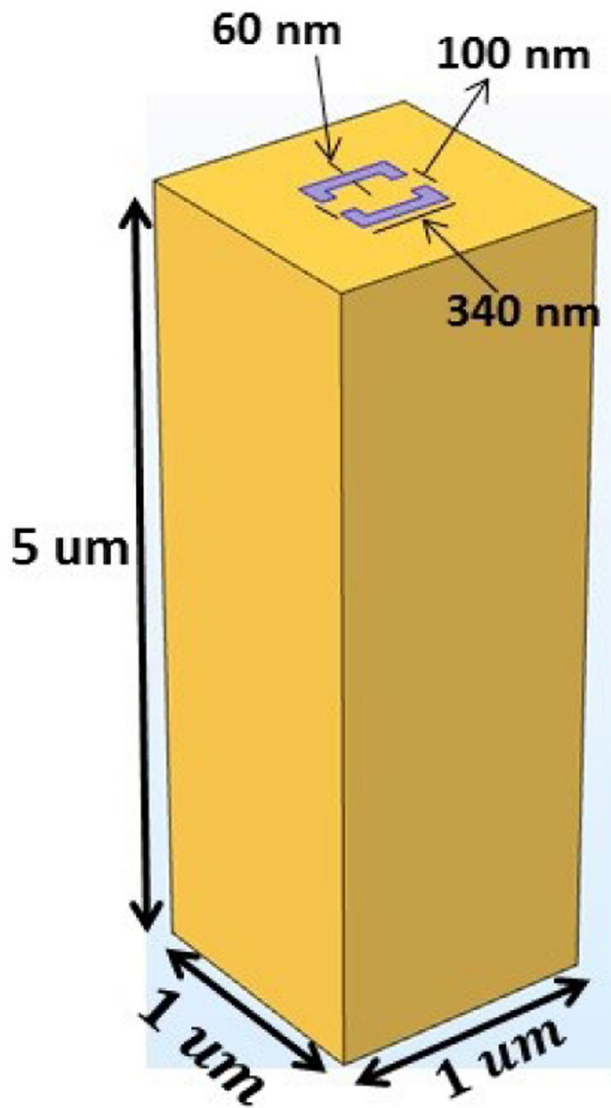
Fig. 6 The sensor unit cell dimensions for operation at a high-frequency regime
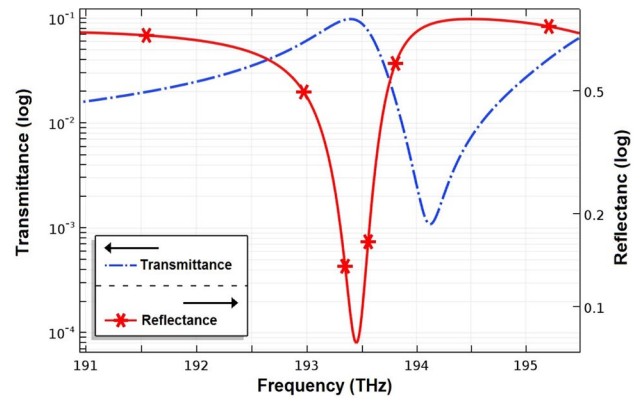


Fig. 7 Transmission and reflection diagram of the proposed sensor at high frequencies

constant and the electrical conductivity of the water. As can be seen, with increasing temperature from 293 to 333 K, the dielectric constant of water decreases from 4.6 to 3.9 and its electrical conductivity rises from 88 to 170 (S/m).

Figure 12 shows temperature changes in the frequency response of the system. According to the simulation results, by increasing temperature, the resonance frequency of the sensor shifts toward higher frequencies (less variation). Also, the transmittance amplitude is reduced, suggesting that the system will have more casualties.

## Sensitivity and FoM

In this section, we will review the operation of the system. For this purpose, we use the sensitivity and FoM parameters. These parameters are defined as Sensivity $= \frac{\Delta\lambda}{\Delta n}$ ($\frac{nm}{RIU}$) and FoM $= \frac{1}{T}\frac{\Delta T}{\Delta n}$, where $\Delta\lambda$, $\Delta T$, and $\Delta n$ represent wavelength, transmittance, and refractive index variations, respectively.

resonant frequency moves toward lower frequencies. At high thicknesses, the changes in the resonant frequency become negligible such that only the transmission amplitude is reduced.

## Temperature

The ambient temperature can affect the response of the system [116, 117]. The fluid part of the blood, which is called plasma, mainly consists of water. Therefore, the temperature can affect this part of the blood and change its dielectric constant. As temperature rises, the real part of the dielectric constant reduces, and the electrical conductivity increases. Figure 11 presents the thermal effects on the dielectric
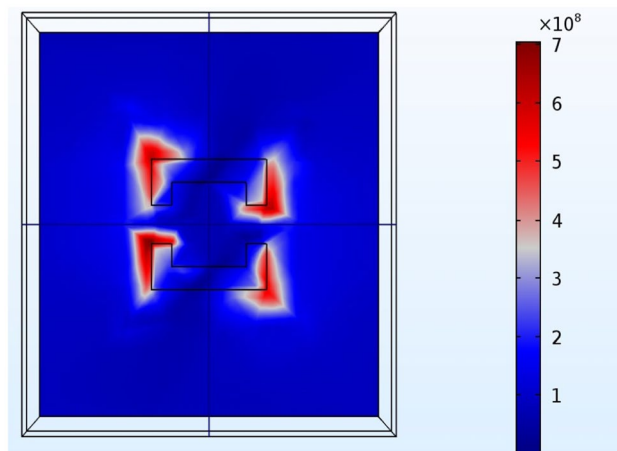


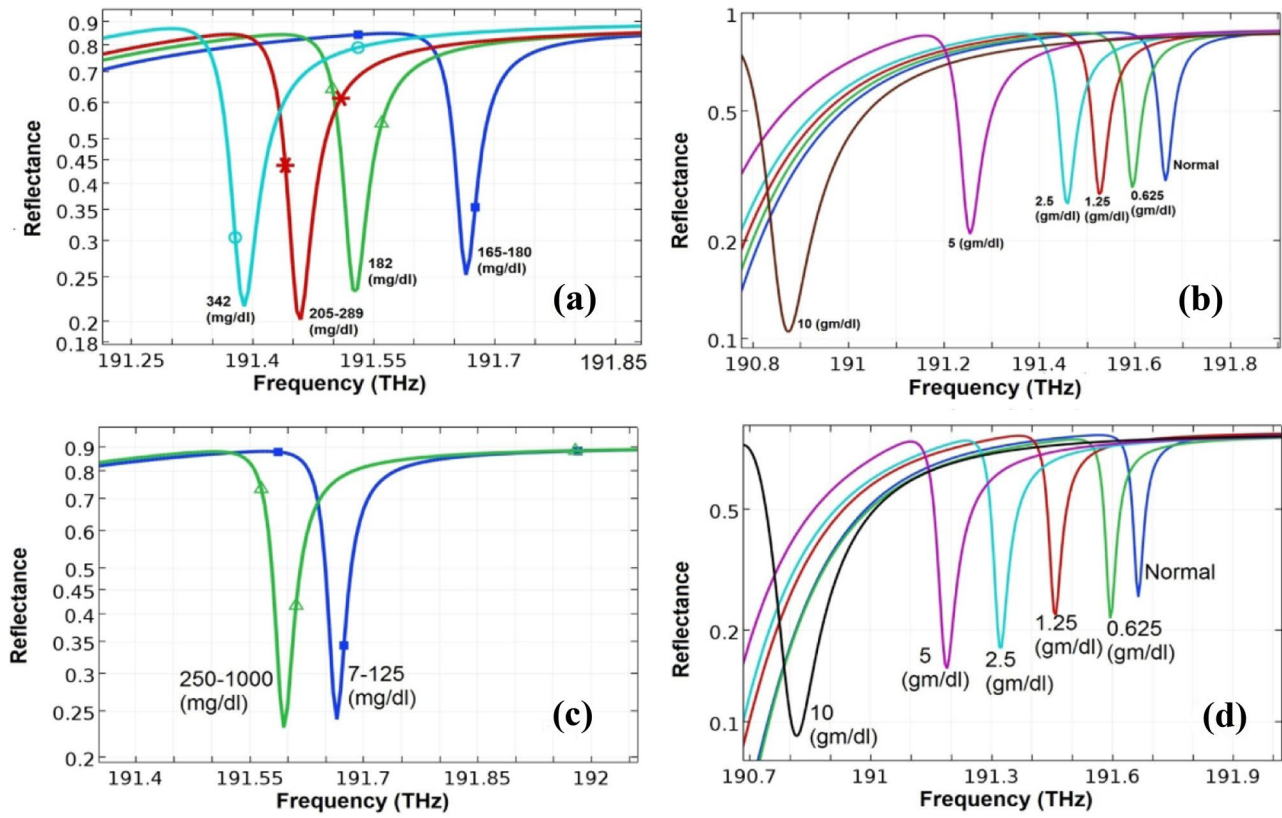Fig. 8 Electric field distribution at $f_r = 193.4$ THz

Fig. 9 Resonance frequency of the proposed system as a function of (**a**) blood glucose concentration, (**b**) urine glucose concentration, (**c**) urine albumin concentration, and (**d**) urine urea concentration

The refractive-index-unit (RIU) is used in optical biosensing, for evanescent wave sensors (optical waveguides, ring resonators, interferometers, and surface plasmon resonance). It is the minimum detectable change in the refractive index of the surface where the evanescent wave is traveling. Also, $T$ is the transmission amplitude at the resonant frequency of the system.
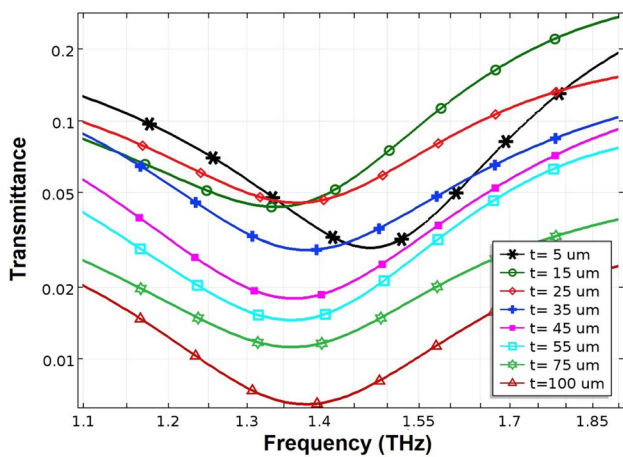
Figure 13a shows the sensitivity and FoM for high-frequency mode and Fig. 13b for low-frequency mode. In high-frequency mode, the maximum sensitivity and FoM are 500 (nm/RIU) and 2000, respectively. These values in the low-frequency mode are 136 (μm/RIU) and 155, respectively.

As we know biosensor in different shapes and mechanism are considered by research groups [26, 118–139]. For example, Wang, Minghua, et al. proposed bimetallic
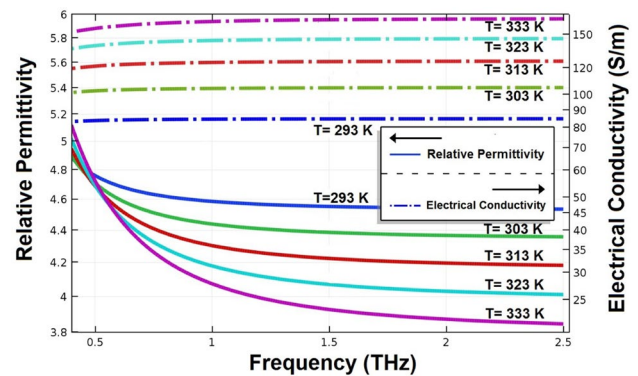


Fig. 10 Effects of sample thickness on the frequency response



Fig. 11 Relative permittivity and electrical conductivity as a function of frequency at different temperatures
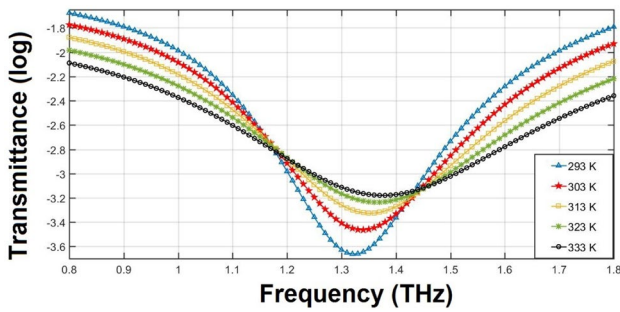
**Fig. 12** Temperature changes versus water frequency response

**Table 2** Comparison between the suggested design and those reported in the literature

| Ref | Structure | Sensitivity (nm/RIU) | FoM | Size (**um²**) |
|-----|-----------|----------------------|-----|----------------|
| [140] | Metasurface | 840 | 84 | 1.1 |
| [141] | Dielectric nanostructures | 263 | 88 | |
| [142] | Photonic crystal | 6.5 | | 12 |
| [143] | Photonic crystal ring resonators | 2500 | 1400 | 13 |
| This work | MMs | 500 | 2000 | 0.34 |

NiFe oxide structures derived from hollow NiFe Prussian blue nanobox for label-free electrochemical biosensing adenosine triphosphate [120]. Jia, Qiaojuan, et al. proposed Polyoxometalate-derived MoS2 nanosheets embedded around iron-hydroxide nanorods as the platform for sensitively determining miRNA-21 [131]. Lu and co-worker proposed numerical investigation of narrowband infrared absorber and sensor based on dielectric-metal metasurface [140]. Almpanis used dielectric nanopatterned surfaces for subwavelength light localization and sensing applications [141].Chopra research group proposed photonic crystal waveguide-based biosensor for detection of diseases [142]. Tavousi research group proposed high sensitivity label-free refractometer-based biosensor applicable to glycated hemoglobin detection in human blood using all-circular photonic crystal ring resonators [143]. Finally, Table 2 compares several types of biosensors with different structures.

**Fig. 13** Sensitivity and FoM of the proposed system for (**a**) low-frequency mode and (**b**) high-frequency mode
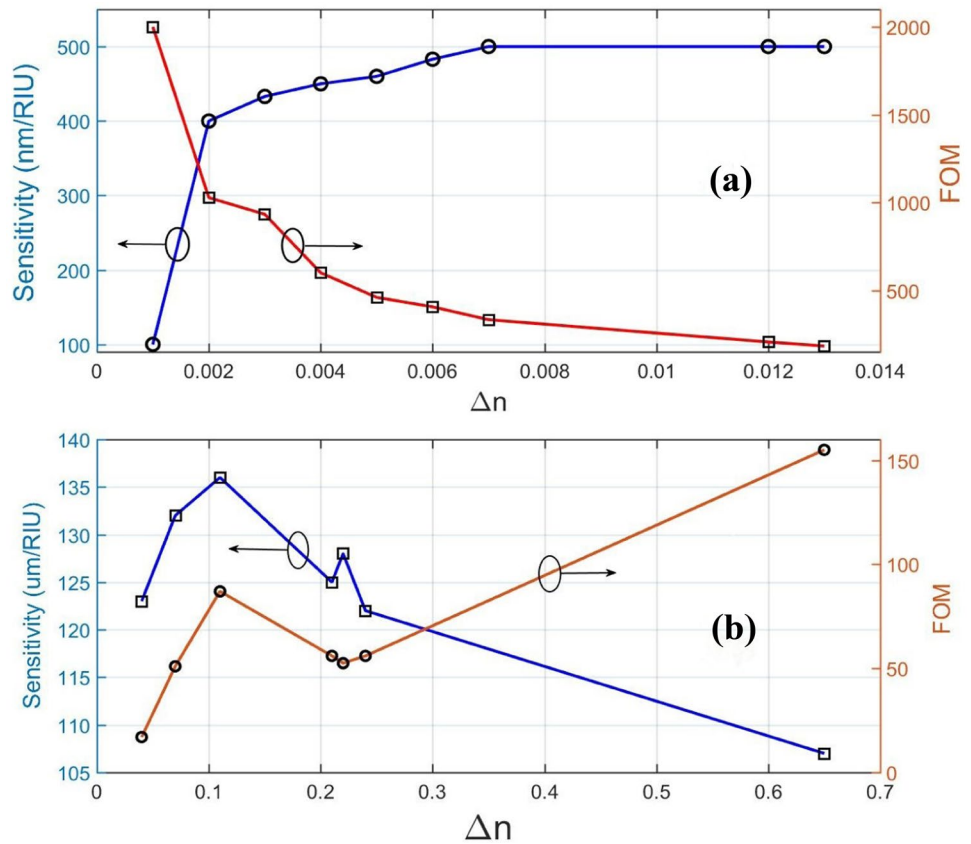
# Conclusion

A biosensor was designed to detect blood components and also to measure the concentration of glucose, albumin, and urea in urine and blood. One of the most important features of this sensor is the easy adjustment, which was demonstrated in the present article, as well. To illustrate this important feature, we set the sensor to operate at low frequencies (around 1 THz) and high frequencies (about 193 THz) and then measured different samples. According to the simulation results, the maximum sensitivity at high-frequency is 500 (nm/RIU) and at low frequency is 136 (um/RIU). Also, FoM in the high frequency is 2000 and in the low frequency is 155. The major features of this biosensor include real-time measurement, high speed, very small dimensions, cost-effectiveness, and free-label of the sample.

**Author Contribution** Hamed Emami Nejad: Software, Data curation, Investigation. Ali Mir: Conceptualization, Methodology, Writing—review and editing. Ali Farmani: Validation, Data curation, Writing—original draft.

## Declarations

**Ethical Approval** This is a numerical study on plasmonic biosensors.

**Consent to Participate** This is a theoretical study on the design of plasmonic biosensors.

**Consent for Publication** All authors of this paper agree to publish our theoretical research.

# References

1. Stanford JL, Stephenson RA, Coyle LM, Cerhan J, Correa R, Eley J, Gilliland F, Hankey B, Kolonel L, Kosary C et al (1973–1995) Prostate cancer trends, seer program, national cancer institute, NIH pub (99–4543)
2. Su F et al (2019) Aptamer-templated silver nanoclusters embedded in zirconium metal–organic framework for targeted antitumor drug delivery. Microporous Mesoporous Mater 275:152–162
3. Wang M et al (2019) Covalent organic framework-based electrochemical aptasensors for the ultrasensitive detection of antibiotics. Biosens Bioelectron 132:8–16
4. Wang Y et al (2020) Design strategy of barium titanate/polyvinylidene fluoride-based nanocomposite films for high energy storage. J Mater Chem A Mater A 8(3):884–917
5. Sun L et al (2018) Early monitoring of rebar corrosion evolution based on FBG sensor. Int J Struct Stab Dyn 18(08):1840001
6. Li C et al (2020) Experimental investigation and error analysis of high precision FBG displacement sensor for structural health monitoring. Int J Struct Stab Dyn 20(06):2040011
7. Zhang C et al (2019) Fibre Bragg grating sensor-based damage response monitoring of an asymmetric reinforced concrete shear wall structure subjected to progressive seismic loads. Struct Control Health Monit 26(3):e2307
8. Zhang C, Jinping Ou (2015) Modeling and dynamical performance of the electromagnetic mass driver system for structural vibration control. Eng Struct 82:93–103
9. Sun L et al (2019) Superwide-range fiber bragg grating displacement sensor based on an eccentric gear: Principles and experiments. J Aerosp Eng 32(1):04018129
10. Sun L et al (2019) The strain transfer mechanism of fiber bragg grating sensor for extra large strain monitoring. Sensors 19(8):1851
11. Song Y et al (2020) Ultrasensitive detection of bisphenol A under diverse environments with an electrochemical aptasensor based on multicomponent AgMo heteronanostructure. Sensors Actuators B Chem 321:128527
12. Rakhshani MR, Mansouri-Birjandi MA (2018) Engineering hexagonal array of Nanoholes for high sensitivity biosensor and application for human blood group detection. IEEE Trans Nanotechnol 17(3):475–481
13. Liu L et al (2018) Effects of arbuscular mycorrhizal inoculation and biochar amendment on maize growth, cadmium uptake and soil cadmium speciation in Cd-contaminated soil. Chemosphere 194:495–503
14. Lin J et al (2020) Controllable antibacterial and bacterially anti-adhesive surface fabricated by a bio-inspired beetle-like macromolecule. Int J Biol Macromol 157:553–560
15. Lin J et al (2020) Anti-liquid-interfering and bacterially antiadhesive strategy for highly stretchable and ultrasensitive strain sensors based on Cassie-Baxter wetting state. Adv Funct Mater 30(23):2000398
16. Zhong P et al (2020) Electrochemically enabled synthesis of sulfide imidazopyridines via a radical cyclization cascade. Green Chem 22(19):6334–6339
17. Feng S et al (2020) Analysis of microplastics in a remote region of the Tibetan Plateau: Implications for natural environmental response to human activities. Sci Total Environ 739:140087
18. Peipei T et al (2020) Large decrease in streamflow and sediment load of Qinghai-Tibetan Plateau driven by future climate change: a case study in Lhasa River Basin. Catena 187:104340
19. Hongwei L et al (2020) Patch aggregation trends of the global climate landscape under future global warming scenario. Int J Climatol 40(5):2674–2685
20. Lv Z, Qiao L (2020) Analysis of healthcare big data. Future Gener Comput Syst 109:103–110
21. Lv Z, Xiu W (2019) Interaction of edge-cloud computing based on SDN and NFV for next generation IoT. IEEE Internet Things J 7(7):5706–5712
22. Lv Z, Song H (2019) Mobile internet of things under data physical fusion technology. IEEE Internet Things J 7(5):4616–4624
23. Lv Z, Kumar N (2020) Software defined solutions for sensors in 6G/IoE. Comput Commun 153:42–47
24. Kiani S, Rezaei P, Karami M, Sadeghzadeh R (2018) Band-stop filter sensor based on siw cavity for the non-invasive measuring of blood glucose. IET Wireless Sensor Systems 9(1):1–5
25. Zhiting W et al (2020) High-temperature persistent luminescence and visual dual-emitting optical temperature sensing in self activated CaNb2O6: Tb3+ phosphor. J Am Ceram Soc
26. Zhang J, Liu B (2019) A review on the recent developments of sequence-based protein feature extraction methods. Curr Bioinform 14(3):190–199
27. Lei X, Jiang S, Zou Q (2020) An in silico approach to identification, categorization and prediction of nucleic acid binding proteins. bioRxiv
28. Jia L et al (2020) Structure design of MoS 2@ Mo 2 C on nitrogen-doped carbon for enhanced alkaline hydrogen evolution reaction. J Mater Sci 55(34):16197–16210

29. Zhang Y et al (2020) Emergence of skyrmionium in a two-dimensional CrGe (Se, Te) 3 Janus monolayer. Phys Rev B 102(24):241107

30. Zhu S et al (2020) Synchronous measuring of triptolide changes in rat brain and blood and its application to a comparative pharmacokinetic study in normal and Alzheimer's disease rats. J Pharm Biomed Anal 185:113263

31. Zhu S et al (2020) Quadruplex stable isotope derivatization strategy for the determination of panaxadiol and panaxatriol in foodstuffs and medicinal materials using ultra high performance liquid chromatography tandem mass spectrometry. J Chromatogr A 1616:460794

32. Wang, Peng et al. Superhydrophobic flexible supercapacitors formed by integrating hydrogel with functional carbon nanomaterials. Chin J Chem

33. Fan Z et al. (2020) Facile synthesis of sulfur@ titanium carbide Mxene as high performance cathode for lithium-sulfur batteries. Nanophotonics 1.ahead-of-print

34. Tahmasebpour M, Bahrami M, Asgari A (2014) Design study of nanogratingbased surface plasmon resonance biosensor in the near-infrared wavelength. Appl Opt 53(7):1449–1458

35. Soni A, Jha SK, Saliva based noninvasive optical urea biosensor, in, (2017) IEEE SENSORS. IEEE 2017:1–3

36. Danaie M, Kiani B (2018) Design of a label-free photonic crystal refractive index sensor for biomedical applications. Photonics Nanostruct Fundam Appl 31:89–98

37. Madadi Z, Abedi K, Darvish G, Khatir M, An infrared narrow-band plasmonic perfect absorber as a sensor, Optik

38. Lai W-C, Chakravarty S, Zou Y, Guo Y, Chen RT (2013) Slow light enhanced sensitivity of resonance modes in photonic crystal biosensors. Appl Phys Lett 102(4):041111

39. Gao N et al (2016) Ultralow frequency acoustic bandgap and vibration energy recovery in tetragonal folding beam phononic crystal. Int J Mod Phys B 30(18):1650111

40. Salim A, Lim S (2018) Review of recent metamaterial microfluidic sensors. Sensors 18(1):232

41. Gao N, Kuan L (2020) An underwater metamaterial for broadband acoustic absorption at low frequency. Appl Acoust 169:107500

42. Gao, Nansha et al. Design, fabrication and sound absorption test of composite porous metamaterial with embedding I-plates into porous polyurethane sponge. Appl Acoust 175: 107845

43. Cao S, Shao Y, Wang Y, Wu T, Zhang L, Huang Y, Zhang F, Liao C, He J, Wang Y (2018) Highly sensitive surface plasmon resonance biosensor based on a low-index polymer optical fiber. Opt Express 26(4):3988–3994

44. Wu D, Tian J, Li L, Yang R (2018) Plasmon induced transparency and refractive index sensing in a new type of graphene-based plasmonic waveguide. Opt Commun 412:41–48

45. Algorri J, Zografopoulos D, Ferraro A, Garcia-Camara B, Vergaz R, Beccherelli R, Sanchez-Pena J (2019) Anapole modes in hollow nanocuboid dielectric metasurfaces for refractometric sensing. Nanomaterials 9(1):30

46. Salemizadeh M, Mahani FF, Mokhtari A (2019) Design of aluminum-based nanoring arrays for realizing efficient plasmonic sensors. JOSA B 36(3):786–793

47. Farmani A (2019) Three-dimensional fdtd analysis of a nanostructured plasmonic sensor in the near-infrared range. JOSA B 36(2):401–407

48. Baqir M, Farmani A, Fatima T, Raza M, Shaukat S, Mir A (2018) Nanoscale, tunable, and highly sensitive biosensor utilizing hyperbolic metamaterials in the near-infrared range. Appl Opt 57(31):9447–9454

49. Farmani A, Mir A, Bazgir M, Zarrabi FB (2018) Highly sensitive nano-scale plasmonic biosensor utilizing fano resonance metasurface in thz range: numerical study. Physica E 104:233–240

50. Hu P et al (2020) Distribution characteristics of salt-out particles in steam turbine stage. Energy 192:116626

51. Yang Y et al (2020) Adsorption behaviors of shale oil in kerogen slit by molecular simulation. Chem Eng J 387:124054

52. Wang X et al (2018) Hierarchical coral-like NiMoS nanohybrids as highly efficient bifunctional electrocatalysts for overall urea electrolysis. Nano Res 11(2):988–996

53. Liu G et al (2017) Antibacterial activity and mechanism of bifidocin A against Listeria monocytogenes. Food Control 73:854–861

54. Jiang D et al (2020) Bioenergetic crosstalk between mesenchymal stem cells and various ocular cells through the intercellular trafficking of mitochondria. Theranostics 10(16):7260

55. Pan D et al (2020) COCO enhances the efficiency of photoreceptor precursor differentiation in early human embryonic stem cell-derived retinal organoids. Stem Cell Res Ther 11(1):1–12

56. Cao B et al (2019) Security-aware industrial wireless sensor network deployment optimization. IEEE Trans Industr Inform 16(8):5309–5316

57. Huang Z et al (2020) Influence of the position of artificial boundary on computation accuracy of conjugated infinite element for a finite length cylindrical shell. Acoust Aust 48(2):287–294

58. Qian J et al (2020) Deep-learning-enabled geometric constraints and phase unwrapping for single-shot absolute 3d shape measurement. APL Photonics 5(4):046105

59. Qian J et al (2020) Single-shot absolute 3D shape measurement with deep-learning-based color fringe projection profilometry. Opt Lett 45(7):1842–1845

60. Hu Y et al (2020) Microscopic fringe projection profilometry: A review. Opt Lasers in Eng :106192

61. Zhang J et al (2020) Resolution analysis in a lens-free on-chip digital holographic microscope. IEEE Trans Comput Imaging 6:697–710

62. Zuo C et al (2013) High-speed three-dimensional shape measurement for dynamic scenes using bi-frequency tripolar pulse-width-modulation fringe projection. Opt Lasers in Eng 51(8):953–960

63. Li X et al (2020) Silver-catalyzed decarboxylative allylation of difluoroarylacetic acids with allyl sulfones in water. Chem Asian J 15(7):1175–1179

64. Liu Y et al (2019) Hierarchical nanocomposite electrocatalyst of bimetallic zeolitic imidazolate framework and MoS2 sheets for non-Pt methanol oxidation and water splitting. Appl Catal B Environ 258:117970

65. Alipour A, Farmani A, Mir A (2018) High sensitivity and tunable nanoscale sensor based on plasmon-induced transparency in plasmonic metasurface. IEEE Sens J 18(17):7047–7054

66. Zografopoulos D, Isic G, Vasic B, Ferraro A, Sinatkas G, Kriezis E, Gajic R, Beccherelli R (2018) Electrically tunable solid-state terahertz metamaterial absorbers, in:12th Int Congr Artif Mat Novel Wave Pheno (Metamaterials), IEEE, pp. 471–473

67. Zografopoulos D, Ferraro A, Isic G, Vasic B, Gajic R, Beccherelli R (2016) Tunable terahertz metamaterials based on nematic liquid crystals, in:2016

68. 41st International Conference on Infrared, Millimeter, and Terahertz waves (IRMMW-THz), IEEE, 2016, pp. 1–2

69. Shahzad A, Qasim F, Ahmed S, Naqvi QA (2011) Cylindrical invisibility cloak incorporating pemc at perturbed void region. Prog Electromagn Res 21:61–76

70. Khanjari SP, Jarchi S, Mohammad-Taheri M (2019) Compact and wideband planar loop antenna with microstrip to parallel strip balun feed using metamaterials. AEU Int J Electron Commun 111:152883

71. Rajak N, Chattoraj N, Mark R (2019) Metamaterial cell inspired high gain multiband antenna for wireless applications. AEU Int J Electron Commun 109:23–30

72. Jafari FS, Naderi M, Hatami A, Zarrabi FB (2019) Microwave jerusalem cross absorber by metamaterial split ring resonator

load to obtain polarization independence with triple band application. AEU Int J Electron Commun 101:138–144

73. Pedram K, Nourinia J, Ghobadi C, Pouyanfar N, Karamirad M (2020) Compact and miniaturized metamaterial-based microstrip fractal antenna with reconfigurable qualification. AEU Int J Electron Commun 114:152959

74. Ameen M, Chaudhary RK (2020) Dual-layer and dual-polarized metamaterial inspired antenna using circular-complementary split ring resonator mushroom and metasurface for wireless applications. AEU Int J Electron Commun 113:152977

75. Fan W, Yan B, Wang Z, Wu L (2016) Three-dimensional all-dielectric metamaterial solid immersion lens for subwavelength imaging at visible frequencies. Science Adv 2(8):e1600901

76. Garg P, Jain P (2020) Novel ultrathin penta-band metamaterial absorber, AEU Int J Electron Commun 153063

77. Ling L et al (2020) Combined application of arbuscular mycorrhizal fungi and exogenous melatonin alleviates drought stress and improves plant growth in tobacco seedlings. J Plant Growth Regul : 1–14

78. Chao Z et al (2020) Wide-field high-resolution 3d microscopy with fourier ptychographic diffraction tomography. Opt Lasers in Eng 128:106003

79. Chao Z et al (2020) Transport of intensity equation: a tutorial. Opt Lasers in Eng : 106187

80. Xie J et al (2018) Evaluating the validity of current mainstream wearable devices in fitness tracking under various physical activities: comparative study. JMIR mHealth and uHealth 6(4):e94

81. Zuo C et al (2015) Transport of intensity phase retrieval and computational imaging for partially coherent fields: the phase space perspective. Opt Lasers in Eng 71:20–32

82. Zhang J et al (2020) On a universal solution to the transport-of-intensity equation. Opt Lett 45(13):3649–3652

83. Wang P et al (2020) A superhydrophobic/electrothermal synergistically anti-icing strategy based on graphene composite. Compos Sci Technol 198:108307

84. Zhang W et al (2021) Assessment of FRP–Concrete Interfacial Debonding with Coupled Mixed-Mode Cohesive Zone Model. J Compos Construc 25(2):04021002

85. Wang XF et al (2020) Predicting Thermophilic Proteins by Machine Learning. Curr Bioinformatics 15(5):493–502

86. Zou Q et al (2019) Gene2vec: gene subsequence embedding for prediction of mammalian N6-methyladenosine sites from mRNA. Rna 25(2):205–218

87. Chen S, Hassanzadeh-Aghdam MK, Ansari R (2018) An analytical model for elastic modulus calculation of SiC whisker-reinforced hybrid metal matrix nanocomposite containing SiC nanoparticles. J Alloys Compd 767:632–641

88. Azad AK, Taylor AJ, Smirnova E, OHara JF (2008) Characterization and analysis of terahertz metamaterials based on rectangular split-ring resonators, Appl Phys Lett 92 (1)011119

89. Emami-Nejad H, Mir A (2017) Design and simulation of a flexible and ultrasensitive biosensor based on frequency selective surface in the microwave range. Opt Quant Electron 49(10):320

90. Wang B-X, Zhai X, Wang G-Z, Huang W-Q, Wang L-L (2015) A novel dualband terahertz metamaterial absorber for a sensor application. J Appl Phys 117(1):014504

91. Sreekanth KV, Alapan Y, ElKabbash M, Ilker E, Hinczewski M, Gurkan UA, De Luca A, Strangi G (2016) Extreme sensitivity biosensing platform based on hyperbolic metamaterials. Nat Mater 15(6):621

92. Lin J et al (2020) Thermo and light-responsive strategies of smart titanium-containing composite material surface for enhancing bacterially anti-adhesive property. Chem Eng J 407:125783

93. Hu J et al (2019) A new anti-biofilm strategy of enabling arbitrary surfaces of materials and devices with robust bacterial anti-adhesion via a spraying modified microsphere method. J Mater Chem A 7(45):26039–26052

94. Zhang W et al (2020) Progress of ethylene action mechanism and its application on plant type formation in crops. Saudi J Biol Sci 27(6):1667–1673

95. Xu W, Xie L, Zhu J, Xu X, Ye Z, Wang C, Ma Y, Ying Y (2016) Gold nanoparticle-based terahertz metamaterial sensors: mechanisms and applications. Acs Photonics 3(12):2308–2314

96. Mirzaei S, Green NG, Rotaru M, Pu SH (2017) Detecting and identifying dna via the thz backbone frequency using a metamaterial-based label-free biosensor, in: Terahertz, RF, Millimeter, and Submillimeter-Wave Technology and Applications X, Vol. 10103, Int Soc Opt Photon, p. 101031I

97. Nejad HE, Mir A, Farmani A, Supersensitive and tunable nanobiosensor for cancer detection, IEEE Sensors Journal

98. La Spada L, Bilotti F, Vegni L (2011) Metamaterial biosensor for cancer detection. SENSORS. IEEE, IEEE, pp 627–630

99. McCutcheon S, Blanco ARA, Houston EF, de Wolf C, Tan BC, Smith A, Groschup MH, Hunter N, Hornsey VS, MacGregor IR et al (2011) All clinically-relevant blood components transmit prion disease following a single blood transfusion: a sheep model of vcjd. PLoS ONE 6(8):e23169

100. Gusev SI, Demchenko PS, Fedorov V, Khodzitsky M, Cherkasova O (2018) Influence of glucose concentration on blood optical properties in THz frequency range. Chin Opt 11(2):182–189

101. Pandey R, Paidi SK, Valdez TA, Zhang C, Spegazzini N, Dasari RR, Barman I (2017) Noninvasive monitoring of blood glucose with Raman spectroscopy. Acc Chem Res 50(2):264–272

102. Robinson S, Dhanlaksmi N (2017) Photonic crystal based biosensor for the detection of glucose concentration in urine. Photonic Sensors 7(1):11–19

103. Tao H, Chieffo LR, Brenckle MA, Siebert SM, Liu M, Strikwerda AC, Fan K, Kaplan DL, Zhang X, Averitt RD et al (2011) Metamaterials on paper as a sensing platform. Adv Mater 23(28):3197–3201

104. Yaxin D et al (2020) Mechanisms and modelling of phosphorus solid–liquid transformation during the hydrothermal processing of swine manure. Green Chem 22.17:5628–5638

105. Han C et al (2019) Spatially distributed crop model based on remote sensing. Agri Water Manage 218:165–173

106. He Li, Chen Y, Li J (2018) A three-level framework for balancing the tradeoffs among the energy, water, and air-emission implications within the life-cycle shale gas supply chains. Resour Conserv Recycl 133:206–228

107. Cheng X et al (2016) Optimal water resources management and system benefit for the Marcellus shale-gas reservoir in Pennsylvania and West Virginia. J Hydrol 540:412–422

108. Chen Y et al (2018) Multi-criteria design of shale-gas-water supply chains and production systems towards optimal life cycle economics and greenhouse gas emissions under uncertainty. Comput Chem Eng 109:216–235

109. Chen Y et al (2017) Life cycle assessment of greenhouse gas emissions and water-energy optimization for shale gas supply chain planning based on multi-level approach: Case study in Barnett, Marcellus, Fayetteville, and Haynesville shales. Energy Convers Manag 134:382–398

110. Chen Y et al (2021) Coupling system dynamics analysis and risk aversion programming for optimizing the mixed noise-driven shale gas-water supply chains. J Clean Prod 278:123209

111. Li X et al (2019) Influence of NbC particles on microstructure and mechanical properties of AlCoCrFeNi high-entropy alloy coatings prepared by laser cladding. J Alloys Compd 788:485–494

112. Liu H et al (2020) Preparation of a hydrophilic and antibacterial dual function ultrafiltration membrane with

quaternized graphene oxide as a modifier. J Colloid Interface Sci 562:182–192

113. Ju Y, Shen T, Wang D (2020) Bonding behavior between reactive powder concrete and normal strength concrete. Constr Build Mater 242:118024

114. Reid CB, Reese G, Gibson AP, Wallace VP (2013) Terahertz time-domain spectroscopy of human blood. IEEE J Biomed Health Inform 17(4):774–778

115. Topsakal E, Karacolak T, Moreland EC (2011) Glucose-dependent dielectric properties of blood plasma, in, XXXth URSI General Assembly and Scientific Symposium. IEEE 2011:1–4

116. Chao C et al (2020) Hot isostatic pressing of a near α-Ti alloy: Temperature optimization, microstructural evolution and mechanical performance evaluation. Mater Sci Eng A :140426

117. Zhang C-W, Jin-Ping Ou, Zhang J-Q (2006) Parameter optimization and analysis of a vehicle suspension system controlled by magnetorheological fluid dampers. Structural Control and Health Monitoring: The Official Journal of the International Association for Structural Control and Monitoring and of the European Association for the Control of Structures 13(5):885–896

118. Wang M et al (2019) Construction of Tb-MOF-on-Fe-MOF conjugate as a novel platform for ultrasensitive detection of carbohydrate antigen 125 and living cancer cells. Biosens Bioelectron 142:111536

119. Wang M et al (2019) Bimetallic cerium and ferric oxides nanoparticles embedded within mesoporous carbon matrix: electrochemical immunosensor for sensitive detection of carbohydrate antigen 19–9. Biosens Bioelectron 135:22–29

120. Wang M et al (2018) Bimetallic NiFe oxide structures derived from hollow NiFe Prussian blue nanobox for label-free electrochemical biosensing adenosine triphosphate. Biosens Bioelectron 113:16–24

121. Qiu T et al (2019) Deep learning: a rapid and efficient route to automatic metasurface design. Adv Sci 6(12):1900128

122. Sun H et al (2019) High-resolution anisotropic prestack Kirchhoff dynamic focused beam migration. IEEE Sens J 20(20):11753–11760

123. Shi M et al (2020) 3D assembly of MXene-stabilized spinel ZnMn2O4 for highly durable aqueous zinc-ion batteries. Chem Eng J 399:125627

124. Wang J et al (2020) Effect analysis on thermal behavior enhancement of lithium–ion battery pack with different cooling structures. J Ener Sto 32:101800

125. Yongfei Y et al (2015) New pore space characterization method of shale matrix formation by considering organic and inorganic pores. J Nat Gas Sci Eng 27:496–503

126. Nansha G et al Hybrid composite meta-porous structure for improving and broadening sound absorption. Mech Syst Signal Process 154:107504

127. Nansha G et al (2020) Teaching-learning-based optimization of a composite metastructure in the 0–10 kHz broadband sound absorption range. J Acoust Soc Am 148.2:EL125-EL129

128. Xue Z et al (2020) The modeling of the electric heating and cooling system of the integrated energy system in the coastal area. J Coast Res 103.SI:1022–1029

129. Chao Y, Gao F, Dong M (2020) Energy efficiency modeling of integrated energy system in coastal areas. J Coast Res 103. SI:995–1001

130. Liu Y et al (2019) Novel and efficient synthesis of Ag-ZnO nanoparticles for the sunlight-induced photocatalytic degradation. Appl surf sci 476:632–640

131. Jia Q et al (2020) Polyoxometalate-derived MoS2 nanosheets embedded around iron-hydroxide nanorods as the platform for sensitively determining miRNA-21. Sensors Actuators B Chem 323:128647

132. Yu H et al (2020) The NOx degradation performance of nano-TiO2 coating for asphalt pavement. Nanomaterials 10(5):897

133. He L et al (2019) Titanium dioxide encapsulated carbon-nitride nanosheets derived from MXene and melamine-cyanuric acid composite as a multifunctional electrocatalyst for hydrogen and oxygen evolution reaction and oxygen reduction reaction. Appl Catal B Environ 248:366–379

134. Shi M et al (2020) 3D interpenetrating assembly of partially oxidized MXene confined Mn–Fe bimetallic oxide for superior energy storage in ionic liquid. Electrochimica Acta 334:135546

135. Zhao X et al (2020) Construction of electric vehicle driving cycle for studying electric vehicle energy consumption and equivalent emissions. Environ Sci Pollut Res 27(30):37395–37409

136. Lv Q et al (2020) Multiscale analysis on spatiotemporal dynamics of energy consumption CO2 emissions in China: Utilizing the integrated of DMSP-OLS and NPP-VIIRS nighttime light datasets. Sci Total Environ 703:134394

137. Zhu L, Kong L, Zhang C (2020) Numerical study on hysteretic behaviour of horizontal-connection and energy-dissipation structures developed for prefabricated shear walls. Appl Sci 10(4):1240

138. Shi M et al (2020) Porous g-C3N4 and MXene dual-confined FeOOH quantum dots for superior energy storage in an ionic liquid. Adv Sci 7(2):1901975

139. Shaojian Q et al (2020) Consensus modeling with asymmetric cost based on data-driven robust optimization. Group Decis Negot 1–38

140. Lu X, Zhang T, Wan R, Xu Y, Zhao C, Guo S (2018) Numerical investigation of narrowband infrared absorber and sensor based on dielectric-metal metasurface. Opt Express 26(8):10179–10187

141. Almpanis E, Papanikolaou N (2016) Dielectric nanopatterned surfaces for subwavelength light localization and sensing applications. Microelectron Eng 15(159):60–63

142. Chopra H, Kaler RS, Painam B (2016) Photonic crystal waveguide-based biosensor for detection of diseases. J Nanophotonics 10(3):036011

143. Tavousi A, Rakhshani MR, Mansouri-Birjandi MA (2018) High sensitivity label-free refractometer based biosensor applicable to glycated hemoglobin detection in human blood using all-circular photonic crystal ring resonators. Opt Commun 15(429):166–174